NeuroImage: Clinical 18 (2018) 963–971

Contents lists available at ScienceDirect

NeuroImage: Clinical

journal homepage: www.elsevier.com/locate/ynicl

Postmortem diffusion MRI of the entire human spinal cord at microscopic resolution

Evan Calabrese[a,b,*], Syed M. Adil[b,d], Gary Cofer[b], Christian S. Perone[c], Julien Cohen-Adad[c], Shivanand P. Lad[d], G. Allan Johnson[b]

[a] Department of Radiology & Biomedical Imaging, University of California San Francisco, San Francisco, CA, USA
[b] Center for In Vivo Microscopy, Duke University Medical Center, Durham, NC, USA
[c] NeuroPoly Lab, Institute of Biomedical Engineering, Polytechnique Montreal, Montreal, QC, Canada
[d] Department of Neurosurgery, Duke University Medical Center, Durham, NC, USA

ARTICLE INFO

Keywords:
Spinal cord
Magnetic resonance microscopy
Tractography
Human
Gray matter

ABSTRACT

The human spinal cord is a central nervous system structure that plays an important role in normal motor and sensory function, and can be affected by many debilitating neurologic diseases. Due to its clinical importance, the spinal cord is frequently the subject of imaging research. Common methods for visualizing spinal cord anatomy and pathology include histology and magnetic resonance imaging (MRI), both of which have unique benefits and drawbacks. Postmortem microscopic resolution MRI of fixed specimens, sometimes referred to as magnetic resonance microscopy (MRM), combines many of the benefits inherent to both techniques. However, the elongated shape of the human spinal cord, along with hardware and scan time limitations, have restricted previous microscopic resolution MRI studies (both *in vivo* and *ex vivo*) to small sections of the cord. Here we present the first MRM dataset of the entire postmortem human spinal cord. These data include 50 μm isotropic resolution anatomic image data and 100 μm isotropic resolution diffusion data, made possible by a 280 h long multi-segment acquisition and automated image segment composition. We demonstrate the use of these data for spinal cord lesion detection, automated volumetric gray matter segmentation, and quantitative spinal cord morphometry including estimates of cross sectional dimensions and gray matter fraction throughout the length of the cord.

1. Introduction

The spinal cord is an essential part of the central nervous system that is responsible for transmitting neuronal signals between the brain and body. In addition to its role as the primary conduit for sensory and motor function, the spinal cord is affected by several debilitating human diseases including multiple sclerosis, amyotrophic lateral sclerosis, and various forms of spinal cord injury (Minagar and Rabinstein, 2012). Lesions to the spinal cord can produce a range of symptoms including pain, paresthesias, weakness, and paralysis. Because of its clinical importance, the spinal cord is frequently a target for imaging research (Wheeler-Kingshott et al., 2014). Historically, light microscopy-based histology has been the major imaging modality used for investigating the spinal cord (Fix, 2008; Sengul et al., 2013; Standring, 2016; Watson et al., 2009). One of the most widely known histological atlases of the spinal cord is *Gray's Anatomy* (Standring, 2016) (now in its 41st edition), which has since been digitized to create a white matter atlas of the human spinal cord (Lévy et al., 2015). A more recent landmark histological atlas is the *Atlas of the Spinal Cord of the Rat, Mouse, Marmoset, Rhesus, and Human* (Sengul et al., 2013). These histologic studies offer sub-cellular in-plane resolution and many unique contrasts based on chemical (*e.g.* cresyl violet) and immunohistochemical (*e.g.* acetylcholinesterase) tissue stains.

While histology remains the gold standard for anatomic and pathologic studies of the spinal cord, it is not without limitations. Histological techniques are labor intensive and require destruction of the sample due to the need for tissue sectioning. The resulting tissue slices are frequently affected by distortions from fixation, embedding, and sectioning. Moreover, each piece of tissue can be stained only once, thus limiting what can be visualized with any given specimen. For these reasons, histologic studies are typically limited to a small number of individual slices, often with large intervening gaps, and therefore lack the ability to represent the three-dimensional anatomy and connectivity of the cord. For example, Gray's Anatomy includes only a single slice through the cervical cord (C4), and the Sengul et al. atlas, one of the most comprehensive of its kind, includes only one slice for each of the

* Corresponding author at: Department of Radiology & Biomedical Imaging, University of California San Francisco, San Francisco, CA, USA.
E-mail address: edc15@duke.edu (E. Calabrese).

https://doi.org/10.1016/j.nicl.2018.03.029
Received 17 October 2017; Received in revised form 15 January 2018; Accepted 21 March 2018
Available online 27 March 2018

31 vertebral levels. Most clinical pathologic assessments of the spinal cord are similarly sparse in their sampling and can potentially miss focal lesions, which may occur anywhere throughout the length of the cord.

Magnetic resonance imaging (MRI) of the spinal cord can overcome many of the drawbacks inherent to conventional histology, albeit at the cost of lower in-plane spatial resolution. Contiguous 3D images can be acquired along the full cord, and multiple contrasts can be visualized within the same tissue. Notably, several MRI contrasts, including diffusion MRI (dMRI), are quantitative and provide additional information about tissue microstructure that is beyond the actual image resolution. However, techniques for spinal cord MRI have historically been limited; in particular, troublesome factors include the spinal cord's small cross-sectional area, artifacts from adjacent bone-soft tissue interfaces, and physiologic motion of blood and cerebrospinal fluid (Cohen-Adad and Wheeler-Kingshott, 2014). Despite these challenges, there have been many notable *in vivo* MRI studies of the human spinal cord including those utilizing dMRI, though they are limited in slice number and resolution (Farrell et al., 2008; Massire et al., 2016; Rasoanandrianina et al., 2017; Taso et al., 2014).

Postmortem microscopic resolution MRI of fixed specimens, sometimes referred to as magnetic resonance microscopy (MRM), offers an alternative approach that addresses many of the limitations of other spinal cord imaging modalities. Using exogenous contrast agents, long scan times, and specialized equipment, superior resolution and contrast can be achieved along the entire cord while maintaining most of the benefits inherent to MRI. Previous MRM studies of the human spinal cord have demonstrated the incredible three-dimensional anatomic detail that this technique can provide, but they have typically been confined to small sections of the cord due to hardware limitations (Bergers et al., 2002; Bot et al., 2004; Gilmore et al., 2009; Mottershead et al., 2003; Nijeholt et al., 2001). Here, we present the first microscopic resolution dMRI dataset of the entire postmortem human spinal cord, made possible by multi-segment acquisition and automated image composition. These data offer a unique opportunity to explore the three-dimensional anatomy and connectivity of the spinal cord at unprecedented resolution. We further demonstrate the use of these data for both pathologic lesion detection and for automated volumetric gray matter segmentation and morphometric analysis using a recently published deep learning method (Perone et al., 2017).

2. Materials and methods

2.1. Specimen procurement

An entire human spinal cord, from pyramidal decussation to cauda equina, was obtained from a deceased adult male in his sixties at the time of death, with no known history of neurologic disease. After death and prior to spinal cord removal, the cadaver was gravity perfused with isotonic saline through the right carotid artery until all visible blood was flushed from the vascular system. The time between death and spinal cord harvest (postmortem interval) was approximately 18 h, and during this time the cadaver was maintained at 4°C. Spinal cord extraction was performed by a trained neurosurgeon using standard surgical instruments and took approximately 1 h to complete. The dissected cord measured approximately 46 cm from pyramidal decussation to filum terminalis.

2.2. Specimen preparation

Immediately after extraction, the dura was opened longitudinally and the spinal cord was sutured to a block of closed-cell polystyrene foam in a fully extended position *via* the attached dural flaps. This was done to ensure that the cord remained straight and suspended during subsequent fixation. The specimen was immersion-fixed in a 10% formalin solution for two weeks at 4 °C and then transferred to a

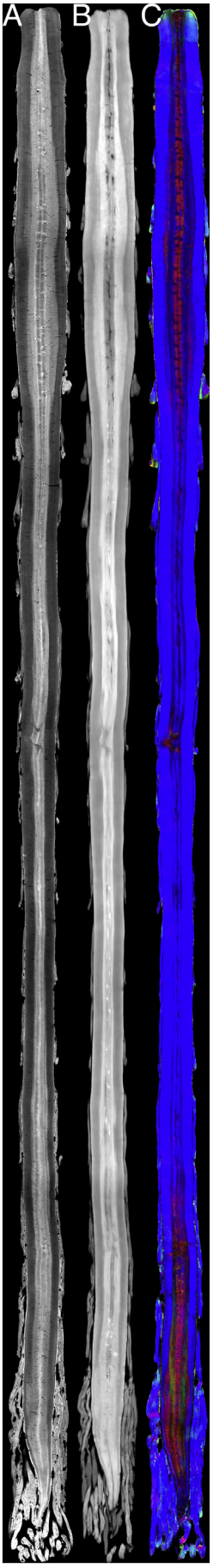

(caption on next page)

Fig. 1. Coronal magnetic resonance microscopy images of the whole human spinal cord at the level of the central canal. Three different image contrasts are included: A) T2*-weighted gradient echo; B) isotropic diffusion-weighted image; C) directionally colored fractional anisotropy.

phosphate-buffered saline solution doped with 2.5 mM gadoteridol for one additional week prior to scanning. Immediately prior to scanning, the spinal cord was completely dissected away from the dura, placed in a custom-fabricated plastic specimen tube, and immersed in Galden HT-200 liquid fluorocarbon (Solvay, Brussels, Belgium) for magnetic susceptibility matching and to prevent specimen dehydration during scanning.

2.3. Imaging hardware

MR imaging was performed on 7 T horizontal-bore small animal MRI system (Magnex Scientific, Yarton, Oxford, UK), controlled by an Agilent console running VnmrJ 4.0 (Agilent Technologies, Santa Clara, CA, USA). Radiofrequency transmission and reception was accomplished with a custom-made 11 cm long cylindrical quadrature coil with a 3.1 cm inner diameter. The coil was affixed to a custom-fabricated magnet bore gantry insert with a 100 cm long sliding inner specimen tube featuring locking distance marks at precise 1 cm intervals. This device was designed to allow exact specimen translation along the magnet bore while restricting rotation about the Z axis, thus facilitating alignment of multiple segments.

2.4. Image acquisition

MR images of the entire cord were acquired in seven separate overlapping segments. The segment field of view was 8 × 2 × 2 cm with 1 cm of overlap on each end. Between each acquisition, the specimen was advanced precisely 7 cm through the magnet bore using the previously described gantry insert. T2*-weighted anatomic images were acquired using a 3D gradient echo sequence with an acquisition matrix of 1600 × 400 × 400, resulting in 50 μm isotropic resolution. Scan parameters included: TR = 50 ms, TE = 9 ms, flip angle = 60°, bandwidth = 100 kHz, averages = 1. Diffusion-weighted images were acquired using a Stejskal-Tanner diffusion-weighted spin echo sequence with an acquisition matrix of 800 × 200 × 200, resulting in 100 μm isotropic resolution. Scan parameters included: TR = 100 ms, TE = 32 ms, bandwidth = 100 kHz, averages = 1. Diffusion preparation (b = 4000 s/mm^2) was achieved with a pair of half sine gradient pulses of width (δ) = 5 ms, separation (Δ) = 23 ms, and gradient amplitude (G) = 50.4 G/cm. A total of 31 non-collinear diffusion-weighted images and 3 b = 0 s/mm^2 images were acquired for each of the seven segments (Koay, 2011). Per-segment acquisition time was 2 h 22 min for anatomic data and 37 h 46 min for diffusion data, resulting in a total acquisition time of approximately 280 h.

2.5. Image processing and composition

Images were reconstructed, corrected for gradient nonlinearity errors, and digitally combined using a custom-developed image processing pipeline implemented in MATLAB (MathWorks, Natick, MA, USA). Gradient nonlinearity correction code was adapted from the General Electric Gradwarp gradient nonlinearity correction tool (GE, Boston, MA, USA). The spherical harmonic coefficients used for gradient nonlinearity correction were derived empirically based on experiments with a linearity phantom (Supplementary Fig. 1) (Calabrese et al., 2017). Image segments were combined into a single image by automated registration of overlapping segments (ANTs, http://picsl.upenn.edu/software/ants/) and subsequent weighted averaging. A six-parameter linear (rigid) registration was performed on the overlapping 1 cm portions of adjacent segments plus a 2 mm margin to allow for specimen positioning imprecision. We used a four-stage multi-resolution registration strategy with downsampling factors of 8, 4, 2, and 1, and Gaussian smoothing sigmas of 6, 4, 1, and 0 voxels at each level, respectively. The registration converged at each level with less than 1000 iterations. The rotations and translations derived from the registration were then applied to each entire segment. Segments were combined by weighted averaging with a linear weighting profile where the voxels closest to magnet isocenter were assigned a weight of 1 and those farthest from isocenter were assigned a weight of 0. These methods were chosen to produce smooth image intensity across composed image segments, however, both gradient non-linearity correction and coil bias can produce slight image intensity variations at the segment overlaps. The final composite field of view was 46.76 × 2.00 × 1.67 cm after cropping the data to fit.

2.6. Diffusion processing and fiber tracking

Diffusion data processing and tractography were performed in DSI studio (http://dsi-studio.labsolver.org/). Standard diffusion tensor scalar maps were generated including fractional anisotropy (FA), axial diffusivity (AD), radial diffusivity (RD), and mean diffusivity (MD). For tractography, the fiber reconstruction algorithm was Generalized Q-Sampling Imaging (GQI), using default parameters (Yeh et al., 2010). Deterministic fiber tracking was performed with uniform subvoxel seeding throughout the entire cord until 100,000 tracks were generated. Additional tracking parameters included a step size of 50 μm, a minimum length threshold of 1 mm, and a maximum angle threshold of 70°. Deterministic tractography was chosen to highlight dominant pathways without the additional false positive pathways that probabilistic tractography methods often yield (Behrens et al., 2007; Thomas et al., 2014).

2.7. Gray matter volume segmentation

A total of 25 evenly distributed axial slices of the T2*-weighted spinal cord image data were manually segmented into gray matter and non-gray matter by a trained technician. These slices were used to train a recently published state-of-the-art Deep Learning Convolutional Neural Network (CNN) model using dilated convolutions (Krizhevsky et al., 2017; Perone et al., 2017; Yu and Koltun, 2015). The trained model was subsequently used to automatically segment the entire T2*-weighted spinal cord image volume. This segmentation method is also able to accurately segment *in vivo* human spinal cord image data (Perone et al., 2017), and could in theory work for any type of spinal cord MRI if appropriate training data were used. No post-processing methods were employed on the model predictions. A whole cord mask was generated using image thresholding and morphological closing, and a white matter label was created by subtracting the gray matter labels from the whole cord mask.

2.8. Spinal cord morphometry

Several morphometric characteristics of the human spinal cord were measured throughout its length (from pyramidal decussation to conus medullaris) including axial dimensions (anterior/posterior and left/right), cross-sectional area, and gray matter volume fraction. Spinal cord dimensions were determined automatically by computing the tightest possible bounding rectangle for each axial image slice after thresholding out background noise. Cross-sectional area was determined by automatically counting all pixels within the spinal cord on each axial slice, and the multiplying by the pixel dimensions. Gray matter fraction was computed as the number of gray matter pixels divided by the total number of pixels within the spinal cord for each axial slice.

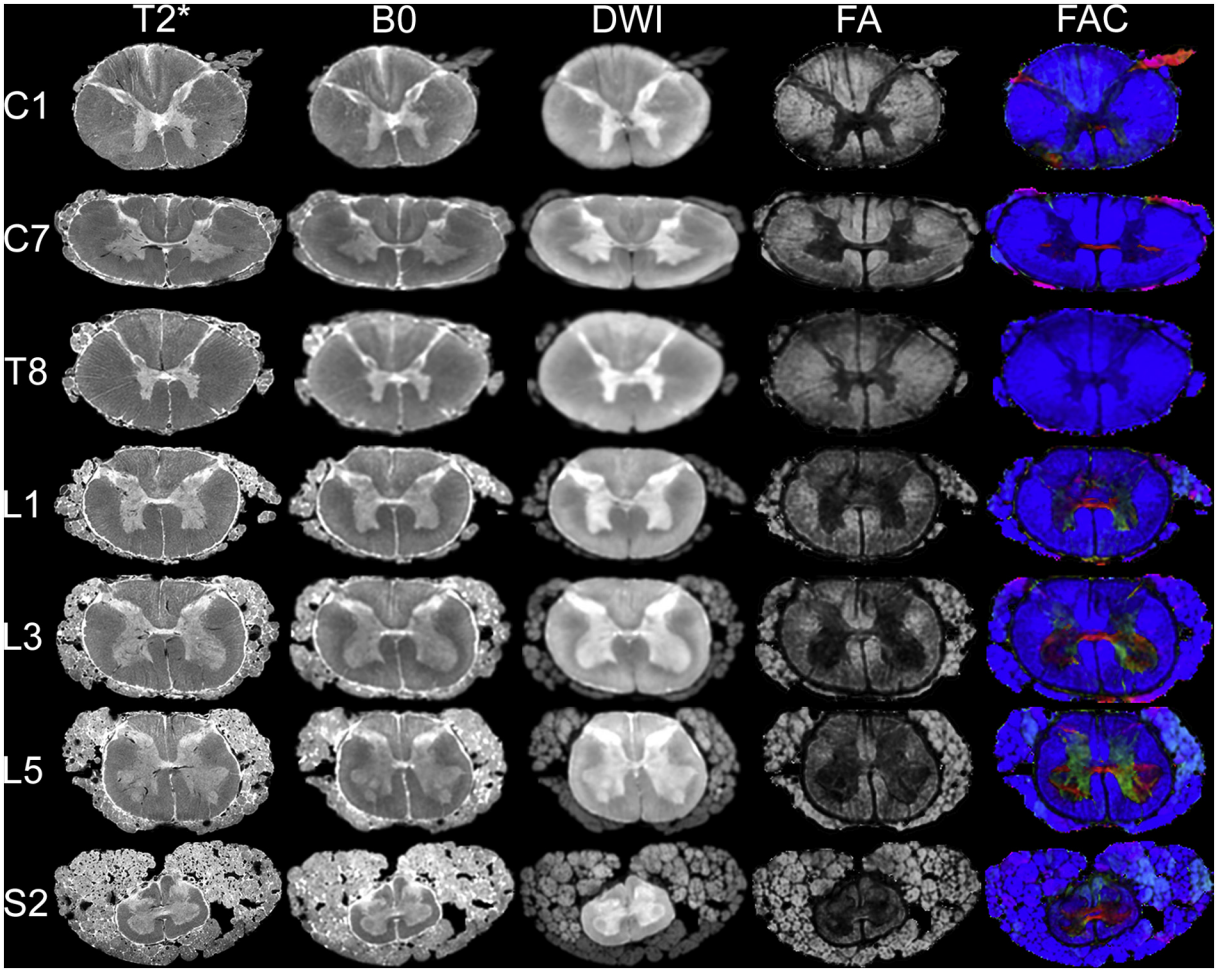

Fig. 2. Multi-contrast axial magnetic resonance microscopy images of the human spinal cord at different levels. Spinal cord levels are named based on the exiting spinal nerves using standard abbreviations: C for cervical, T for thoracic, L for lumbar, and S for sacral. Contrasts include: T2*, T2*-weighted gradient echo; B0, b = 0 image from diffusion acquisition; DWI, isotropic diffusion weighted image; FA, fractional anisotropy; FAC, directionally colored fractional anisotropy.

3. Results

3.1. Image results

The final composite anatomic and diffusion-derived images allow visualization of the entire human spinal cord at spatial resolutions that are currently only achievable in smaller tissue segments (Fig. 1). For the purposes of this study, spinal cord levels are named according to the 31 pairs of exiting spinal nerve roots (8 cervical, 12 thoracic, 5 lumbar, 5 sacral, and 1 coccygeal). The high spatial resolution of the data, combined with the multitude of diffusion-derived image contrasts, provides exceptional anatomic detail at all spinal cord levels (Fig. 2). The data provide high gray matter/white matter contrast, and also resolve several sub-structures including gray matter nuclei and small white matter pathways. For example, in the lumbar gray matter it is possible to resolve both ventral (motor) nuclei, as well as dorsal (sensory) nuclei such as the nucleus proprius/substantia gelatinosa (Fig. 3, right). Small axonal pathways are also visible, particularly on diffusion contrasts, including the anterior gray commissure and dorsal/ventral nerve rootlets (Fig. 3, left). Calculated diffusion tensor scalars were relatively constant along the length of the spinal cord white matter, apart from a slight increase in FA and AD in the lumbar cord relative to the cervical/thoracic cord, and a much larger drop in FA (~50%) and corresponding rise in all diffusivity measures in the distal 15 cm of the cord. Diffusion scalar measurements throughout the length of the spinal cord white matter are presented in Supplementary Fig. 2.

3.2. Spinal cord tractography

Whole spinal cord crossing fiber tractography yielded the expected major white matter pathways within the spinal cord. In addition to those tracks commonly seen in *in vivo* spinal cord tractography (*e.g.* dorsal columns, spinocerebellar, and corticospinal tracts), several smaller white matter pathways are also accurately reconstructed, including the dorsal and ventral nerve rootlets. In the cervical cord, dorsal rootlet tractography reveals the pathways of the dorsal root entry zone (DREZ), which is an important target for functional neurosurgical procedures used to treat certain pain syndromes (Fig. 4A) (Rahimpour and Lad, 2016). The combination of high spatial resolution and crossing fiber tractography models also allows tracking of pathways within the spinal cord gray matter, such as interneuron pathways and the anterior gray commissure (Fig. 4B).

3.3. Characterization of a spinal cord lesion

Despite intentionally procuring the spinal cord specimen from a patient with no known history of neurologic disease, review of the data revealed spinal cord lesion at approximately the 6th thoracic nerve root level (Fig. 5). High-resolution anatomic images show a 5 × 4 × 2 mm unilateral lesion that involves the left dorsal and adjacent white matter pathways. The diffusion characteristics of the lesion include decreased MD and FA compared to adjacent normal appearing white matter. In addition, the axial (primary) diffusivity within the lesion is left-right

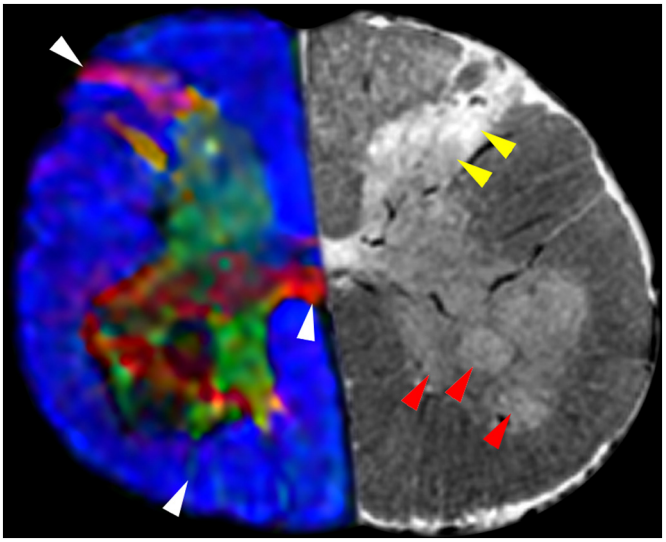

Fig. 3. Axial magnetic resonance microscopy images of the human spinal cord at approximately the 4th lumbar vertebral level. Directionally colored fractional anisotropy (left) reveals small axonal pathways including the anterior gray commissure and dorsal/ventral nerve rootlets (white arrowheads). T2*-weighted gradient echo images demonstrate both ventral (motor) nuclei (red arrowheads), as well as dorsal (sensory) nuclei such as the nucleus proprius/substantia gelatinosa (yellow arrowheads). (For interpretation of the references to color in this figure legend, the reader is referred to the web version of this article.)

oriented (red) in contrast to the craniocaudally oriented (blue) axial diffusivity of adjacent normal thoracic cord. These lesion characteristics are nonspecific, and could be caused by many different forms of spinal cord pathology. Another equally likely possibility is that this lesion occurred postmortem (*e.g.* during specimen extraction), though there was no evidence of external damage to the specimen prior to scanning. Subsequent histologic analysis could have clarified these findings, though it was not performed in this case to avoid specimen destruction.

3.4. Gray matter volumetric segmentation

Automated volumetric gray matter segmentation was found to be highly accurate on manual inspection of the data. The automated segmentation precisely captures even thin gray matter structures such as the gray commissure and dorsal horns. Importantly, the algorithm also performs well in regions with varying gray matter anatomy, such as in the cervical cord where several gray matter columns appear, change in shape, and eventually disappear (Fig. 6). The high-resolution three-dimensional nature of the data also allows highly accurate volumetric measurements and three-dimensional renderings of spinal cord gray matter anatomy (Fig. 6, right column). In this specimen, total gray matter volume was estimated at 3.72 ml, which is in line with prior *in vivo* MRI-based estimates (Fradet et al., 2014).

3.5. Spinal cord morphometry

The results of the morphometric analysis of the spinal cord are presented in Fig. 7. Spinal cord axial dimensions, cross-sectional area, and gray matter volume fraction are displayed from cauda equina (left) to conus medullaris (right). The location of the incidentally discovered spinal cord lesion is marked on the gray matter fraction graph, as it causes a noticeable local distortion in the gray matter fraction without affecting cross-sectional area. These data clearly show the expected cervical and lumbar enlargements of the spinal cord. In addition, they show that the lumbar enlargement is primarily due to an increase in width, with relatively little change in anterior/posterior dimension

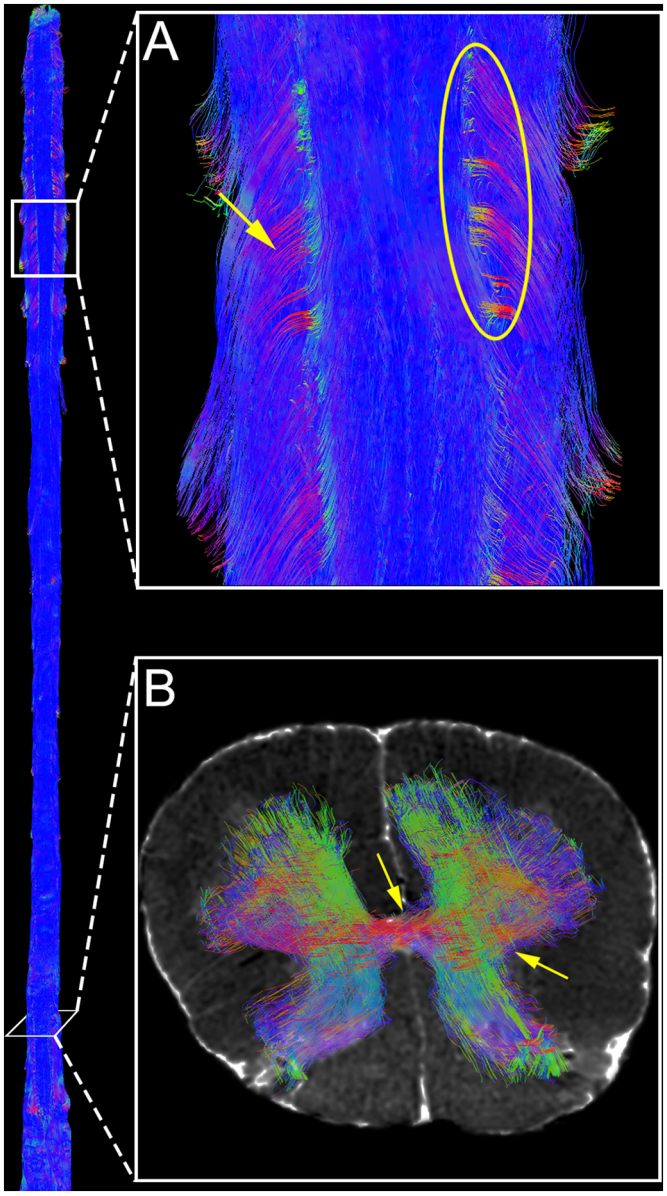

Fig. 4. Directionally colored diffusion tractography of the human spinal cord. A dorsal view of whole spinal cord tractography (left) is provided for orientation. A) Magnified view of the cervical spinal cord shows dorsal nerve rootlets (yellow arrow) and the dorsal root entry zone for the 5th cervical spinal nerve (yellow circle). B) Axial cross-sectional view at approximately the 5th lumbar vertebral level demonstrating gray matter tractography including interneuron pathways and the anterior gray commissure (yellow arrows). Ascending/descending white matter pathways are hidden for clarity. (For interpretation of the references to color in this figure legend, the reader is referred to the web version of this article.)

compared to the thoracic cord (Kameyama et al., 1996). As expected, gray matter fraction is highest in the cervical and lumbar cord, where motor nuclei are relatively large. Perhaps less intuitively, the gray matter fraction is highest in the conus medullaris, where there is relatively little white matter, and the gray matter occupies nearly half of the small cross-sectional area of the cord (Kameyama et al., 1996). These MRM derived morphometric measurements are in line with prior studies reporting direct measurement of gross anatomic specimens, accounting for differences in technique (Elliott, 1945; Kameyama et al., 1996; Ko et al., 2004).

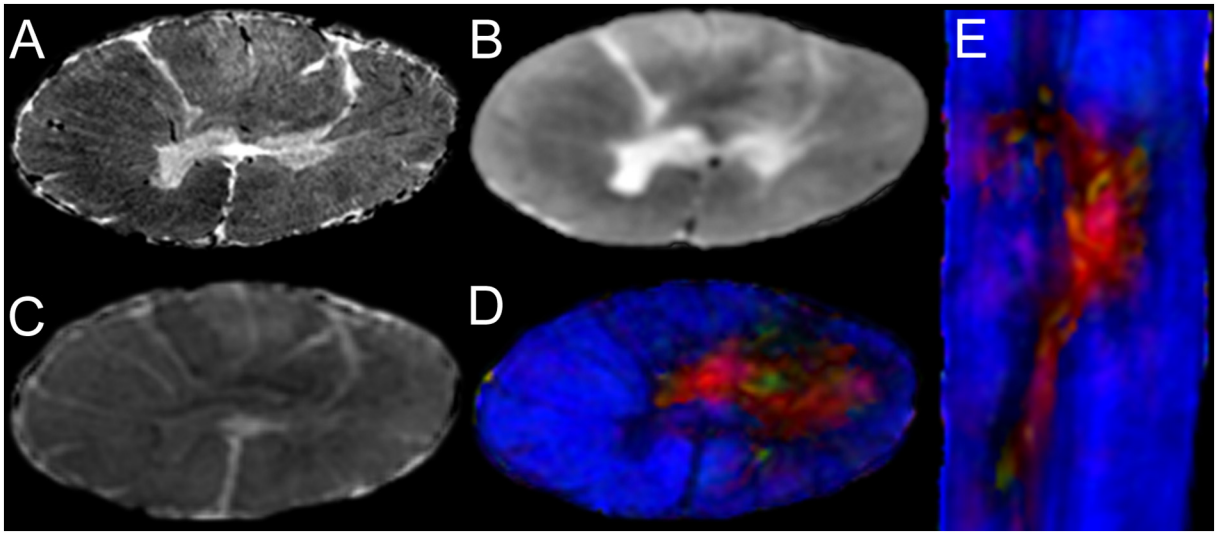

Fig. 5. Magnetic resonance microscopy images of an incidentally discovered 5 × 4 × 2 mm unilateral lesion that obliterates the dorsal horn but spares many peripheral white matter pathways. The lesion has decreased diffusivity and reduced FA compared to adjacent white matter, and a left-right (red) oriented axial diffusivity. A) axial T2*-weighted gradient echo; B) axial isotropic diffusion-weighted image; C) axial apparent diffusion coefficient image; D) axial directionally colored fractional anisotropy (FAC) image; E) sagittal FAC. (For interpretation of the references to color in this figure legend, the reader is referred to the web version of this article.)

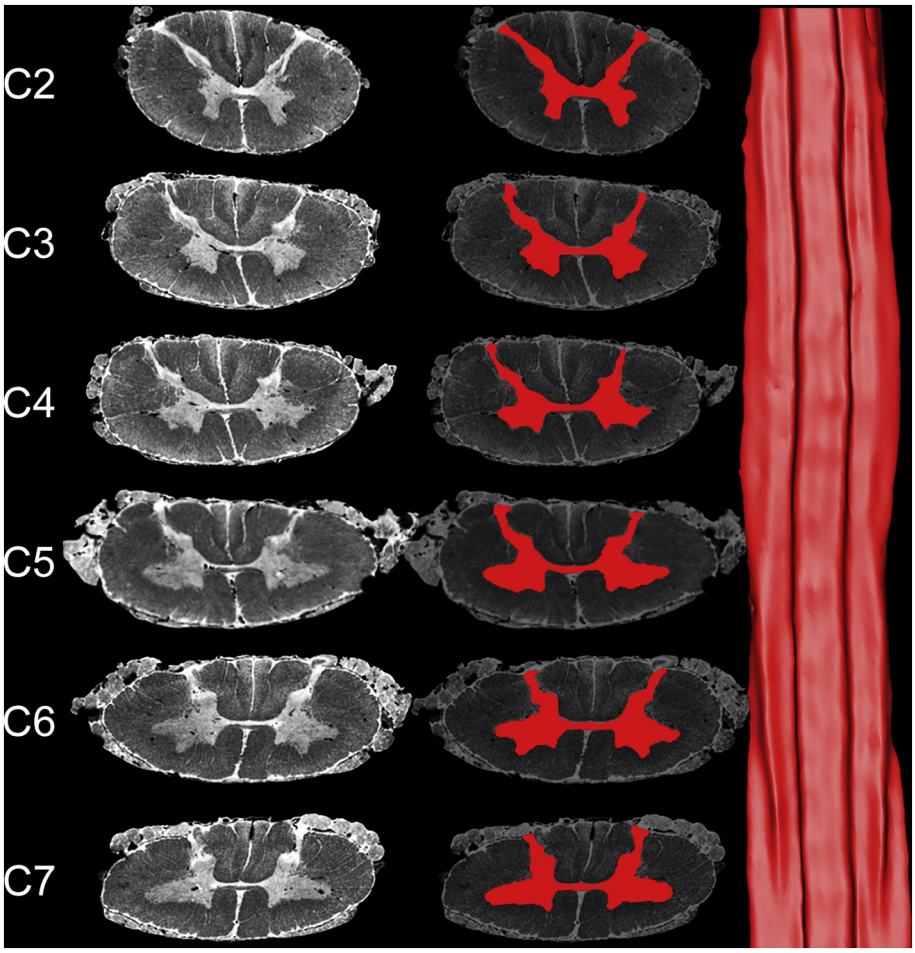

Fig. 6. Automated gray matter segmentation results in the cervical spinal cord. Standard spinal cord segment abbreviations are used including C for cervical segments. Axial T2*-weighted anatomic images (left column) are shown with their corresponding automated gray matter segmentations (center column) and a ventral view of a three-dimensional rendering of the cervical gray matter segmentation (right column).

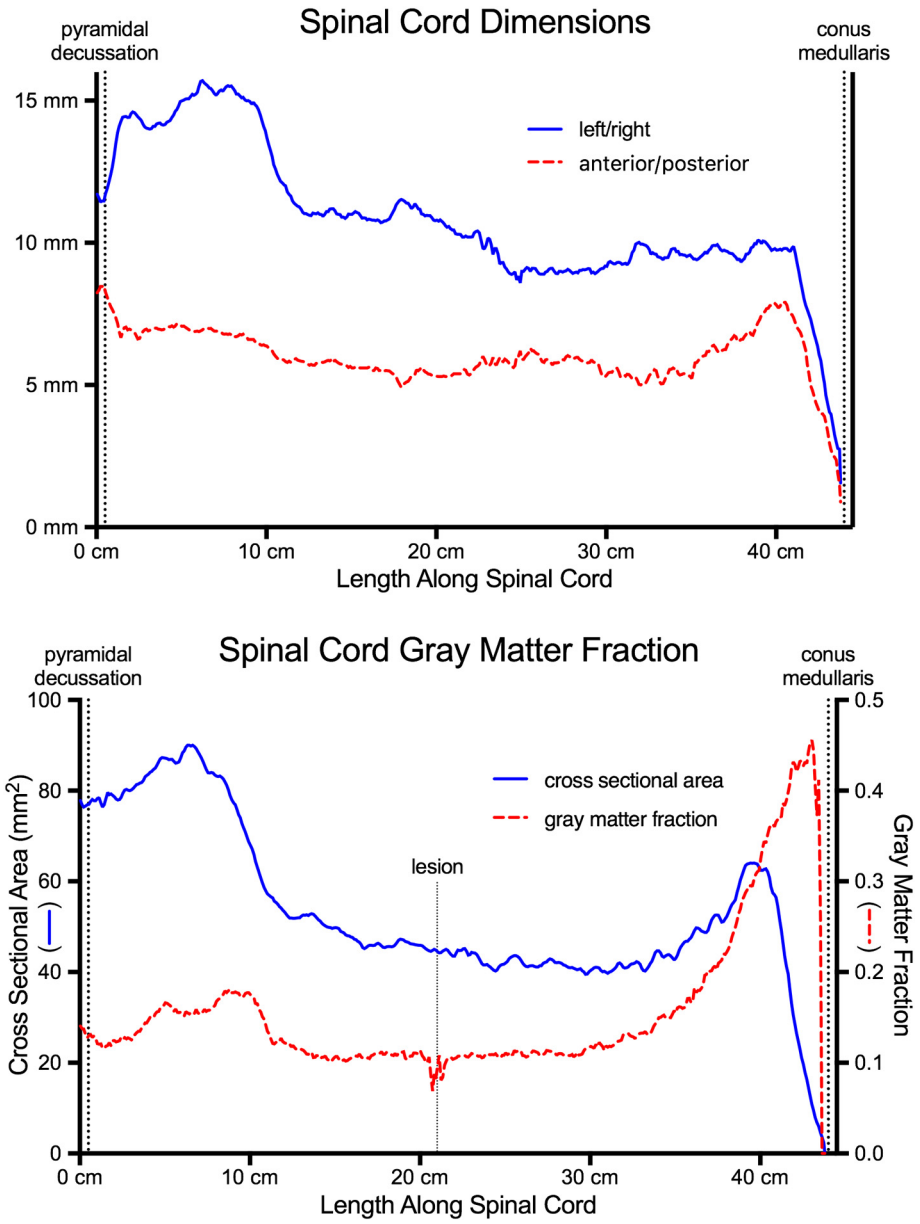

Fig. 7. Morphometric analysis of the human spinal cord throughout its length. Spinal cord axial dimensions (top), cross-sectional area (bottom, left axis), and gray matter fraction (bottom, right axis) are plotted from pyramidal decussation (left) to conus medullaris (right). The location of an incidentally discovered spinal cord lesion is marked on the gray matter fraction plot as it produces a noticeable local distortion in the gray matter fraction without significantly affecting cross-sectional area.

4. Discussion

Here we present the first microscopic resolution dMRI dataset of the entire postmortem human spinal cord, generated with multi-segment MRM acquisition and an automated image composition pipeline. These techniques allow for image quality and resolution that far exceed the current state of the art for *in vivo* MRI studies. For example, Farrel et al. imaged 30 axial slices using q-space analysis and a 3 T scanner with eight healthy volunteers and four multiple sclerosis (MS) patients, resulting in a diffusion-weighted image (DWI) resolution of $1.3 \times 1.3 \times 3.0$ mm, though data was restricted to the cervical cord (Farrell et al., 2008). Taso et al. created a probabilistic atlas and anatomical template of the human cervical and thoracic spinal cord at 3 T based on data from 15 healthy volunteers at a better resolution of $0.5 \times 0.5 \times 5.0\,mm^2$, but this was only made possible by taking just one slice at each vertebral level (and excluding most of the lumbar cord) (Taso et al., 2014). Using a 7 T field and 10 healthy volunteers, Massire et al. achieved a resolution of $0.18 \times 0.18 \times 3\,mm^3$ for T_2*-weighted gradient recalled echo (GRE) and $0.8 \times 0.8 \times 3\,mm^3$ for DWI, but data were again limited to 12 slices localized in the cervical cord (Massire et al., 2016). Obviously, there are fundamental differences between *in vivo* and postmortem imaging, and comparisons between the two must be taken in context.

In addition to *in vivo* studies, several groups have previously reported postmortem MRM studies of the spinal cord. Most prior postmortem studies have been performed on small animals and non-human primates including rats (Ford et al., 1994; Gulani et al., 2001; Kozlowski et al., 2008; Nevo et al., 2001; Schwartz et al., 1999), cats (Cohen-Adad et al., 2008; Pattany et al., 1997), vervet monkeys (Lundell et al., 2011), and marmosets (Fujiyoshi et al., 2007). Human spinal cord MRM studies have also been previously reported; however, they have largely focused on small segments of the spinal cord (2–6 cm)

from patients with pathology (often MS) and at lower spatial resolutions than the data presented here (Bergers et al., 2002; Bot et al., 2004; Gilmore et al., 2009; Mottershead et al., 2003; Nijeholt et al., 2001). To our knowledge, this study represents the first microscopic-resolution MRI dataset of the entire human spinal cord. It is also one of the few such studies to image a specimen without known neurologic disease. These data provide a unique look at the normal anatomy and connectivity of the human spinal cord. They also demonstrate the level of detail that can be expected from studies using similar techniques on specimens with known neurologic disease.

There are multiple other potential applications of this work. Previously, our group has used similar postmortem imaging techniques on a human brainstem and thalamus specimen (Calabrese et al., 2015). The resulting dataset was registered to *in vivo* clinical images from patients who had undergone deep brain stimulation for essential tremor, and it was demonstrated that positive treatment outcomes correlated with stimulator lead proximity to the dentatorubrothalamic tract as illustrated on the postmortem template. We anticipate that similar data from the spinal cord could likewise be used to improve modeling of fiber activation/inhibition for spinal cord stimulators and other spinal neuroprostheses. Additionally, spinal cord dMRI may be used to model the fiber anatomy associated with other neurosurgical procedures, such as nucleus caudalis dorsal root entry zone lesioning for atypical facial pain syndromes (Rahimpour and Lad, 2016). It is conceivable that having a high-resolution template for the fiber anatomy could enhance neurosurgical planning for this procedure.

The techniques presented here could also be used for postmortem pathologic assessment of the spinal cord at autopsy. MRM not only allows small spinal cord lesion detection, but can also provide quantitative morphometry and volume estimates. The automated segmentation and morphometric analysis presented here yielded results that are similar to previous experiments based on manual measurement of individual tissue slices (Elliott, 1945; Kameyama et al., 1996; Ko et al., 2004). Compared to one of the most comprehensive prior studies (Kameyama et al., 1996), our absolute measurements are slightly larger, which is likely explained by differences in fixation technique (*i.e.* 10% *vs* 20% formalin solution); however, our results were generated using automated rather than manual methods, and include nearly 150-fold more data points (*i.e.* one data point per 0.1 mm compared to one per spinal cord segment). The automated throughput and increased granularity of MRM based morphometry may provide additional sensitivity for detecting structural spinal cord pathology (Fujiwara et al., 1988; Ogino et al., 1983). Unfortunately, this method is limited to postmortem specimens, and spinal cord extraction can be time consuming, taking approximately 1 h in this case. However, extraction is currently required for microscopic evaluation of spinal cord pathology, whether by conventional histology or by MRM. Importantly, due to its non-destructive nature, MRM can be performed on specimens in addition to conventional histologic assessment.

This study has several important limitations. First, postmortem fixation is known to induce structural changes in neurologic tissue. For example, a previous MRM study of cervical spinal cord segments found that tissue fixation resulted in disproportionally reduced longitudinal diffusivity (but not radial diffusivity or anisotropy) (Kim et al., 2009). Similar observations have been made in animal studies comparing fresh and fixed central nervous system tissue (Pattany et al., 1997; Sun et al., 2005). Postmortem interval is also known to affect the diffusion properties of central nervous system tissue, even when relatively short (*e.g.* 4–6 h) (Miller et al., 2011; Shepherd et al., 2009). These microstructural changes are likely similar than those accompanying traditional histological techniques, and the reduction in tissue diffusivity is countered to some extent by the use of a higher *b*-value (Dyrby et al., 2010). Second, the use of only 30 diffusion directions limits the ability to detect intravoxel fiber crossing, and tractography results must be interpreted in this context. Third, while necessary for this study, multi-segment acquisition and image composition can potentially induce registration errors and resolution non-linearity at segment overlaps. Fourth, this study includes only a single specimen, and an unexpected spinal cord lesion was identified, which reduces the generalizability of these data. Finally, the acquisition time for these data was quite long (~280 h). Fortunately, more efficient pulse sequences and compressed sensing techniques promise to address this limitation (Wang et al., 2017).

In conclusion, we have presented the first microscopic resolution dMRI dataset of the entire postmortem human spinal cord. In addition to its utility as a basic research tool, this work has applications in pathologic evaluation, atlas generation, and surgical planning. More broadly, this study is important in improving our understanding of the three-dimensional structure of the human spinal cord. While this study has notable limitations, it remains one of the most comprehensive studies of its kind in the human spinal cord. We hope that by making these images publically available, other groups will find new and innovative uses for the data that far exceed what has been discussed here.

Supplementary data to this article can be found online at https://doi.org/10.1016/j.nicl.2018.03.029.

Acknowledgements

This work was supported by the National Institutes of Health [grant numbers P41 EB015897 and 1S10OD010683-01]. We would like to acknowledge John Nouls, Yi Qi, Shervin Rahimpour, and Jason Talbott for their contributions to this work.

References

Behrens, T.E.J., Berg, H.J., Jbabdi, S., Rushworth, M.F.S., Woolrich, M.W., 2007. Probabilistic diffusion tractography with multiple fibre orientations: what can we gain? NeuroImage 34, 144–155. http://dx.doi.org/10.1016/j.neuroimage.2006.09.018.

Bergers, E., Bot, J.C.J., van der Valk, P., Castelijns, J.A., Lycklama a Nijeholt, G.J., Kamphorst, W., Polman, C.H., Blezer, E.L.A., Nicolay, K., Ravid, R., Barkhof, F., 2002. Diffuse signal abnormalities in the spinal cord in multiple sclerosis: direct postmortem in situ magnetic resonance imaging correlated with in vitro high-resolution magnetic resonance imaging and histopathology. Ann. Neurol. 51, 652–656. http://dx.doi.org/10.1002/ana.10170.

Bot, J.C.J., Blezer, E.L.A., Kamphorst, W., Lycklama a Nijeholt, G.J., Ader, H.J., Castelijns, J.A., Ig, K.N., Bergers, E., Ravid, R., Polman, C., Barkhof, F., 2004. The spinal cord in multiple sclerosis: relationship of high-spatial-resolution quantitative MR imaging findings to histopathologic results. Radiology 233, 531–540. http://dx.doi.org/10.1148/radiol.2332031572.

Calabrese, E., Hickey, P., Hulette, C., Zhang, J., Parente, B., Lad, S.P., Johnson, G.A., 2015. Postmortem diffusion MRI of the human brainstem and thalamus for deep brain stimulator electrode localization. Hum. Brain Mapp. 36, 3167–3178. http://dx.doi.org/10.1002/hbm.22836.

Calabrese, E., Cofer, G., Lad, S.P., Johnson, G.A., 2017. Diffusion MRI of the Entire Postmortem Human Spinal Cord at Microscopic Resolution. Proceedings of the International Society for Magnetic Resonance in Medicine 25th Annual Meeting, Abstract 0786.

Cohen-Adad, J., Wheeler-Kingshott, C., 2014. Quantitative MRI of the Spinal Cord. Academic Press, San Diego.

Cohen-Adad, J., Descoteaux, M., Rossignol, S., Hoge, R.D., Deriche, R., Benali, H., 2008. Detection of multiple pathways in the spinal cord using q-ball imaging. NeuroImage 42, 739–749. http://dx.doi.org/10.1016/j.neuroimage.2008.04.243.

Dyrby, T.B., Baaré, W.F.C., Alexander, D.C., Jelsing, J., Garde, E., Søgaard, L.V., 2010. An ex vivo imaging pipeline for producing high-quality and high-resolution diffusion-weighted imaging datasets. Hum. Brain Mapp. 32, 544–563. http://dx.doi.org/10.1002/hbm.21043.

Elliott, H.C., 1945. Cross-sectional diameters and areas of the human spinal cord. Anat. Rec. 93, 287–293.

Farrell, J.A.D., Smith, S.A., Gordon-Lipkin, E.M., Reich, D.S., Calabresi, P.A., van Zijl, P.C.M., 2008. High b-value q-space diffusion-weighted MRI of the human cervical spinal cord in vivo: feasibility and application to multiple sclerosis. Magn. Reson. Med. 59, 1079–1089. http://dx.doi.org/10.1002/mrm.21563.

Fix, J., 2008. Atlas of the Human Brain and Spinal Cord. Jones & Bartlett Learning, Burlington.

Ford, J.C., Hackney, D.B., Alsop, D.C., Jara, H., Joseph, P.M., Hand, C.M., Black, P., 1994. MRI characterization of diffusion coefficients in a rat spinal cord injury model. Magn. Reson. Med. 31, 488–494.

Fradet, L., Arnoux, P.-J., Ranjeva, J.-P., Petit, Y., Callot, V., 2014. Morphometrics of the entire human spinal cord and spinal canal measured from in vivo high-resolution anatomical magnetic resonance imaging. Spine 39 (4), E262–E269. http://dx.doi.org/10.1097/BRS.0000000000000125.

Fujiwara, K., Yonenobu, K., Hiroshima, K., Ebara, S., Yamashita, K., Ono, K., 1988.

Morphometry of the cervical spinal cord and its relation to pathology in cases with compression myelopathy. Spine 13, 1212–1216.
Fujiyoshi, K., Yamada, M., Nakamura, M., Yamane, J., Katoh, H., Kitamura, K., Kawai, K., Okada, S., Momoshima, S., Toyama, Y., Okano, H., 2007. In vivo tracing of neural tracts in the intact and injured spinal cord of marmosets by diffusion tensor tractography. J. Neurosci. 27, 11991–11998. http://dx.doi.org/10.1523/JNEUROSCI.3354-07.2007.
Gilmore, C.P., Geurts, J.J.G., Evangelou, N., Bot, J.C.J., van Schijndel, R.A., Pouwels, P.J.W., Barkhof, F., Bö, L., 2009. Spinal cord grey matter lesions in multiple sclerosis detected by post-mortem high field MR imaging. Mult. Scler. 15, 180–188. http://dx.doi.org/10.1177/1352458508096876.
Gulani, V., Webb, A.G., Duncan, I.D., Lauterbur, P.C., 2001. Apparent diffusion tensor measurements in myelin-deficient rat spinal cords. Magn. Reson. Med. 45, 191–195.
Kameyama, T., Hashizume, Y., Sobue, G., 1996. Morphologic features of the normal human cadaveric spinal cord. Spine 21, 1285–1290.
Kim, T.H., Zollinger, L., Shi, X.F., Rose, J., Jeong, E.-K., 2009. Diffusion tensor imaging of ex vivo cervical spinal cord specimens: the immediate and long-term effects of fixation on diffusivity. Anat. Rec. 292, 234–241. http://dx.doi.org/10.1002/ar.20823.
Ko, H.-Y., Park, J.H., Shin, Y.B., Baek, S.Y., 2004. Gross quantitative measurements of spinal cord segments in human. Spinal Cord 42, 35–40. http://dx.doi.org/10.1038/sj.sc.3101538.
Koay, C.G., 2011. A simple scheme for generating nearly uniform distribution of antipodally symmetric points on the unit sphere. J. Comput. Sci. 2, 377–381. http://dx.doi.org/10.1016/j.jocs.2011.06.007.
Kozlowski, P., Raj, D., Liu, J., Lam, C., Yung, A.C., Tetzlaff, W., 2008. Characterizing white matter damage in rat spinal cord with quantitative MRI and histology. J. Neurotrauma 25, 653–676. http://dx.doi.org/10.1089/neu.2007.0462.
Krizhevsky, A., Sutskever, I., Hinton, G.E., 2017. ImageNet classification with deep convolutional neural networks. Commun. ACM 60, 84–90. http://dx.doi.org/10.1145/3065386.
Lévy, S., Benhamou, M., Naaman, C., Rainville, P., Callot, V., Cohen-Adad, J., 2015. White matter atlas of the human spinal cord with estimation of partial volume effect. NeuroImage 119, 262–271. http://dx.doi.org/10.1016/j.neuroimage.2015.06.040.
Lundell, H., Nielsen, J.B., Ptito, M., Dyrby, T.B., 2011. Distribution of collateral fibers in the monkey cervical spinal cord detected with diffusion-weighted magnetic resonance imaging. NeuroImage 56, 923–929. http://dx.doi.org/10.1016/j.neuroimage.2011.02.043.
Massire, A., Taso, M., Besson, P., Guye, M., Ranjeva, J.-P., Callot, V., 2016. High-resolution multi-parametric quantitative magnetic resonance imaging of the human cervical spinal cord at 7T. NeuroImage 143, 58–69. http://dx.doi.org/10.1016/j.neuroimage.2016.08.055.
Miller, K.L., Stagg, C.J., Douaud, G., Jbabdi, S., Smith, S.M., Behrens, T.E.J., Jenkinson, M., Chance, S.A., Esiri, M.M., Voets, N.L., Jenkinson, N., Aziz, T.Z., Turner, M.R., Johansen-Berg, H., McNab, J.A., 2011. Diffusion imaging of whole, post-mortem human brains on a clinical MRI scanner. NeuroImage 57, 167–181. http://dx.doi.org/10.1016/j.neuroimage.2011.03.070.
Minagar, A., Rabinstein, A.A., 2012. Spinal Cord Diseases, an Issue of Neurologic Clinics. Elsevier.
Mottershead, J.P., Schmierer, K., Clemence, M., Thornton, J.S., Scaravilli, F., Barker, G.J., Tofts, P.S., Newcombe, J., Cuzner, M.L., Ordidge, R.J., McDonald, W.I., Miller, D.H., 2003. High field MRI correlates of myelin content and axonal density in multiple sclerosis—a post-mortem study of the spinal cord. Int. J. Neurol. 250, 1293–1301. http://dx.doi.org/10.1007/s00415-003-0192-3.
Nevo, U., Hauben, E., Yoles, E., Agranov, E., Akselrod, S., Schwartz, M., Neeman, M., 2001. Diffusion anisotropy MRI for quantitative assessment of recovery in injured rat spinal cord. Magn. Reson. Med. 45, 1–9.
Nijeholt, G.J., Bergers, E., Kamphorst, W., Bot, J., Nicolay, K., Castelijns, J.A., van Waesberghe, J.H., Ravid, R., Polman, C.H., Barkhof, F., 2001. Post-mortem high-resolution MRI of the spinal cord in multiple sclerosis: a correlative study with conventional MRI, histopathology and clinical phenotype. Brain 124, 154–166.
Ogino, H., Tada, K., Okada, K., Yonenobu, K., Yamamoto, T., Ono, K., Namiki, H., 1983. Canal diameter, anteroposterior compression ratio, and spondylotic myelopathy of the cervical spine. Spine 8, 1–15.
Pattany, P.M., Puckett, W.R., Klose, K.J., Quencer, R.M., Bunge, R.P., Kasuboski, L., Weaver, R.G., 1997. High-resolution diffusion-weighted MR of fresh and fixed cat spinal cords: evaluation of diffusion coefficients and anisotropy. Am. J. Neuroradiol. 18, 1049–1056.
Perone, C.S., Calabrese, E., Cohen-Adad, J., 2017. Spinal Cord Gray Matter Segmentation Using Deep Dilated Convolutions. (arXiv 1710.01269).
Rahimpour, S., Lad, S.P., 2016. Surgical options for atypical facial pain syndromes. Neurosurg. Clin. N. Am. 27, 365–370. http://dx.doi.org/10.1016/j.nec.2016.02.010.
Rasoanandrianina, H., Grapperon, A.-M., Taso, M., Girard, O.M., Duhamel, G., Guye, M., Ranjeva, J.-P., Attarian, S., Verschueren, A., Callot, V., 2017. Region-specific impairment of the cervical spinal cord (SC) in amyotrophic lateral sclerosis: a preliminary study using SC templates and quantitative MRI (diffusion tensor imaging/inhomogeneous magnetization transfer). NMR Biomed. 75, e3801. http://dx.doi.org/10.1002/nbm.3801.
Schwartz, E.D., Yezierski, R.P., Pattany, P.M., Quencer, R.M., Weaver, R.G., 1999. Diffusion-weighted MR imaging in a rat model of syringomyelia after excitotoxic spinal cord injury. Am. J. Neuroradiol. 20, 1422–1428.
Sengul, G., Watson, C., Tanaka, I., Paxinos, G., 2013. Atlas of the Spinal Cord of the Rat, Mouse, Marmoset, Rhesus, and Human. Academic Press, San Diego.
Shepherd, T.M., Flint, J.J., Thelwall, P.E., Stanisz, G.J., Mareci, T.H., Yachnis, A.T., Blackband, S.J., 2009. Postmortem interval alters the water relaxation and diffusion properties of rat nervous tissue—implications for MRI studies of human autopsy samples. NeuroImage 44, 820–826. http://dx.doi.org/10.1016/j.neuroimage.2008.09.054.
Standring, S., 2016. Gray's Anatomy, 41st ed. Elsevier Limited, New York.
Sun, S.-W., Neil, J.J., Liang, H.-F., He, Y.Y., Schmidt, R.E., Hsu, C.Y., Song, S.-K., 2005. Formalin fixation alters water diffusion coefficient magnitude but not anisotropy in infarcted brain. Magn. Reson. Med. 53, 1447–1451. http://dx.doi.org/10.1002/mrm.20488.
Taso, M., Le Troter, A., Sdika, M., Ranjeva, J.-P., Guye, M., Bernard, M., Callot, V., 2014. Construction of an in vivo human spinal cord atlas based on high-resolution MR images at cervical and thoracic levels: preliminary results. MAGMA 27, 257–267. http://dx.doi.org/10.1007/s10334-013-0403-6.
Thomas, C., Ye, F.Q., Irfanoglu, M.O., Modi, P., Saleem, K.S., Leopold, D.A., Pierpaoli, C., 2014. Anatomical accuracy of brain connections derived from diffusion MRI tractography is inherently limited. Proc. Natl. Acad. Sci. U. S. A. 111, 16574–16579. http://dx.doi.org/10.1073/pnas.1405672111.
Wang, N., Cofer, G., Anderson, R.J., Dibb, R., Qi, Y., Badea, A., Johnson, G.A., 2017. Compressed Sensing to Accelerate Connectomic Histology in the Mouse Brain. Proceedings of the International Society for Magnetic Resonance in Medicine 25th Annual Meeting, Abstract 1178.
Watson, C., Paxinos, G., Kayalioglu, G., 2009. The Spinal Cord. Academic Press, San Diego.
Wheeler-Kingshott, C.A., Stroman, P.W., Schwab, J.M., Bacon, M., Bosma, R., Brooks, J., Cadotte, D.W., Carlstedt, T., Ciccarelli, O., Cohen-Adad, J., Curt, A., Evangelou, N., Fehlings, M.G., Filippi, M., Kelley, B.J., Kollias, S., Mackay, A., Porro, C.A., Smith, S., Strittmatter, S.M., Summers, P., Thompson, A.J., Tracey, I., 2014. The current state-of-the-art of spinal cord imaging: applications. NeuroImage 84, 1082–1093. http://dx.doi.org/10.1016/j.neuroimage.2013.07.014.
Yeh, F.-C., Wedeen, V.J., Tseng, W.-Y.I., 2010. Generalized q-sampling imaging. IEEE Trans. Med. Imaging 29, 1626–1635. http://dx.doi.org/10.1109/TMI.2010.2045126.
Yu, F., Koltun, V., 2015. Multi-scale Context Aggregation by Dilated Convolutions. (arXiv 1511.07122).